Materials Science & Engineering A 781 (2020) 139148

Contents lists available at ScienceDirect

Materials Science & Engineering A

journal homepage: http://www.elsevier.com/locate/msea

Ageing response of cold-rolled Al–Cu–Mg alloy

Ivan S. Zuiko *, Rustam Kaibyshev

Belgorod National Research University, Pobeda 85, Belgorod, 308015, Russia

ARTICLE INFO

Keywords:
Aluminium alloys
Thermomechanical processing
Mechanical properties
Precipitation
Deformation structure
Ageing

ABSTRACT

This work presents a detailed investigation of the ageing behaviour of AA2519 alloy subjected to cold rolling with reduction of 10–80% (ε~0.11–1.61). The impact of pre-straining level and ageing duration on the mechanical performance was elucidated *via* hardness and tensile testing, DSC and analytical TEM. The increasing rolling reduction followed by ageing reduces the peak age hardening and pronounces softening under over-ageing. This effect of pre-strain on mechanical properties is related to the dependence of a dispersion of plate-shaped precipitates that form on the $\{001\}_\alpha$ and $\{111\}_\alpha$ planes on deformation structure. The results show that prior plastic strain profoundly changes kinetics of the ageing reaction and precipitation sequence. The peak age hardening is provided by the dense and homogeneous precipitation of a θ'-phase, while the over-ageing is attribute to the concurrent precipitation of the θ-phase on boundaries and thickening θ'-phase plates on dislocations. In addition, an Ω-phase platelets appear during ageing; however, its number density is insufficient to affect the mechanical properties, significantly.

1. Introduction

Thermomechanical processing (TMP) is widely applied to produce high-strength products from age-hardenable aluminium alloys of 2XXX series [1]. It consists of four consecutive operations: a solution treatment followed by quenching, cold working and artificial ageing [1]. Cold working by rolling or stretching accelerates the precipitation process and provides additional strengthening in an overwhelming majority of wrought aluminium alloys [1]. Cold worked ($\varepsilon \leq 0.1$) Al–Cu alloys with small Mg additions exhibit a superior ageing response [1,2]. Pre-straining increases the concentration of crystalline defects (particularly dislocations) and modifies the distribution of secondary phase particles, thereby affecting the coherency, shape, dimensions, aspect ratio, interparticle spacing, volume fraction and number density of the secondary phase particles precipitated during ageing, which improves the strength of above alloys [1,2]. The superposition of dispersion strengthening and dislocation strengthening causes Al–Cu–(Mg) alloys subjected to TMP to exhibit a high mechanical performance [1–8]. Moreover, increasing the rolling reduction is an effective way to increase value of dislocation strengthening and, therefore, the overall strength [3]. Extensive cold rolling with a moderate strain of $\leq$1.4 is commercially viable and can be implemented in the TMP of production lines [1,3,8]. The TMP development with intense plastic pre-straining of Al–Cu–(Mg) alloys is practically attractive for structural applications because of the high strength and sufficient ductility [2,3,5–9]. Dislocation strengthening significantly supplements the strength developed by dispersion strengthening. However, it should be considered that extensive cold working may reduce the dispersion strengthening [3,6].

A moderate-to-high pre-strain induces a specific deformation structure that strongly affects the ageing behaviour [2,3,5–8,10–13]. This occurs during extensive rolling owing to the formation of microshear bands (MBs) and/or lamellar structure with nanoscale interboundary spacings. The previously mentioned structural elements promote the storage of lattice dislocations, which provides very high strain hardening and an acceptable ductility [3,9]. Strain-induced boundaries contribute significantly to the yield stress (σ_{YS}) [3,4]. Therefore, an increasing pre-strain affects the contributions of different strengthening mechanisms to the overall σ_{YS} [3,5,9,12,18]. These contributions were recognized to be additive [3–5,7–18] and expressed as follows:

$$\sigma_{YS} = \sigma_o^{Al} + \sigma_{SS} + \sigma_p + \sigma_{GB} + \sigma_d \quad (1)$$

where σ_o^{Al} is the resistance to dislocation glide in high-purity aluminium, σ_{SS} is the solid solution strengthening attributed to solutes presented inside the aluminium matrix, σ_P is the dispersion strengthening, σ_{GB} is the grain boundary strengthening and σ_d is the dislocation strengthening. Eq. (1) was validated for TMP with small pre-strains [4,12,18]. This additive rule becomes invalid with increasing pre-strain level [13,

* Corresponding author.
E-mail addresses: zuiko_ivan@bsu.edu.ru (I.S. Zuiko), rustam_kaibyshev@bsu.edu.ru (R. Kaibyshev).

https://doi.org/10.1016/j.msea.2020.139148
Received 7 December 2019; Received in revised form 19 February 2020; Accepted 23 February 2020
Available online 26 February 2020

14,18]. The increasing contributions of $\Sigma(\sigma_d+\sigma_{GB})$ to σ_{YS} with increasing strain reduces the value of precipitation strengthening strongly despite the fact that the precipitation strengthening mechanism acts independently and no considerable changes occur in the distribution of secondary precipitations [1,13,14,18].

Literature indicates that the weakening of the age-hardening effect in Al alloys subjected to TMP with large pre-strains can be attributed to the following four factors:

(i) The supersaturation by vacancies and high dislocation density promote a recovery under ageing [19];
(ii) The grain growth during ageing decreases σ_{GB} [19,20];
(iii) The decomposition of supersaturated solid solutions (SSSS) in Al alloys under peak ageing subjected to high strains occurs in a distinctly different way than that of coarsely grained alloys and leads to the formation of thermodynamically stable phases, which do not contribute to dispersion strengthening, at the expense of the strengthening transition phases [8,10–19,21,22];
(iv) The interaction between long-range stress fields originating from stored dislocations and coherent/semicoherent transition phases precipitated on these dislocations decreases the overall internal elastic strain and, therefore, decreases σ_d and σ_P [21].

Evidently, the chemical composition of aluminium alloy and pre-strain level affect the roles of the aforementioned factors in reducing age hardening. According to Refs. [1,3,5,10,11] Cu solutes retard dislocation motion which inhibits a recovery. As a result, high energy dislocation structures inducing long-range strain fields evolve during extensive cold rolling [3]. No significant recovery was observed in Al–Cu–(Mg) alloys under ageing up to 210 °C [6,17]. Whereas grain coarsening was observed only in Al–Cu alloys with nanoscale structures produced by intense pre-straining [7,13,19]. Therefore, factors (i) and (ii) are not important for Al–Cu alloys subjected to cold rolling up to commercially viable reductions [3]. It is apparent that factor (iii) may be responsible for the breakdown of the linear additive law described by Eq. (1) in Al–Cu alloys because the segregations of solutes on strain-induced grain boundaries and Cottrell atmospheres provide additional nucleation sites for the formation of an incoherent θ-phase and semi-coherent θ′-phase, respectively [1,8,14,16,18–20,22–25]. Currently, there is no sufficient information concerning factor (iv).

The aim of the present study was to examine the ageing response of an AA2519 alloy subjected to TMP with pre-strain through extensive cold rolling. Specific attention was given to Eq. (1) with respect to the true pre-strain, ε, ranges from 0.11 to 1.61. The present study is a part of ongoing research devoted to investigating the structure–property relationship and optimising the resulting precipitate dispersion, and ultimately, mechanical properties of modern Al–Cu–Mg alloys. The deformation structure produced by cold rolling and TMP effect at low strain on the precipitation behaviour during ageing were fully studied previously [3,18]. In addition, the precipitation behaviour of this alloy with and without pre-strain was described in Refs. [18,23]. The ageing conditions in previous [18,23] and present studies are identical.

2. Material and experimental procedures

The AA2519 alloy (a nominal chemical composition of Al–5.64Cu–0.33Mn–0.23Mg–0.15Zr–0.11Ti–0.09V–0.08Fe–0.08Zn–0.04Sn–0.01Si; in weight %) was manufactured by semi-continuous casting followed by homogenisation annealing at 510 °C for 24 h [2,18,23]. Billets with dimensions of 100 × 120 × 200 mm^3 were machined from homogenized ingots and isothermally swaged with a total strain of ~1 at a temperature of ~400 °C. Next, the plates with a 45 mm width, 250 mm length and different thickness (3.33–15 mm) were machined from the billets. The thickness was dictated by the rolling reduction. Then the plates were solution heat treated at 530 °C for 1 h and immediately quenched in cold water (~20 °C). Following these, the plates were rolled at room temperature to the reductions ranging from 10 to 80% (logarithmic strain of 0.11–1.61). The final thickness (3 mm) was the same for all plates. Finally, the cold worked plates were aged at 190 ± 1 °C with different durations using a forced-air electric furnace (Memmert Universal Oven model UF55). To interrupt the decomposition process the specimens were quenched in cold (~20 °C) water. In this paper the acronyms "UAC", "PAC" and "OAC" stand for under-, peak- and over-ageing conditions, respectively.

The Vickers microhardness was assessed with a Wilson Wolpert 402MVD tester at a load of 2 N and dwell time of 10 s. The strength and ductility (as a function of the ageing time), were monitored with tensile tests. Flat dog-bone shaped specimens with 25 mm gauge length and dimensions of 3 × 7 mm^2 were machined from the central part of the plates; with an electric discharge sawing machine Sodick AQ300L. The tensile axes of the specimens were parallel to the rolling direction. Subsequently, they were tensioned to failure at room temperature with a screw-driven Instron 5882 testing machine fitted with an automatic high-resolution contacting extensometer MFX 500. The initial strain rate was 1.3 × 10^{-3} s^{-1} and the cross-head speed remained constant. The tensile properties were estimated from stress–strain plots with the standard procedure following from ASTM E8/E8M (Standard Test Methods for Tension Testing of Metallic Materials). At least three samples were tested under each condition to ensure accurate results; the error bars were provided according to the standard deviation. Other mechanical tests details can be found in Refs. [2,18,23].

Transmission electron microscopy (TEM) was conducted with JEOL JEM-2100 and Technai G^2 F20 microscopes. The TEM analysis technique for the examination of secondary phase particles with $\{001\}_\alpha$ and $\{111\}_\alpha$ habit planes was thoroughly described in Refs. [18,23]. To guarantee reproducibility, the diameters and thickness of precipitates were determined as average values of $\geq 10^3$ measurements. Differential scanning calorimetry (DSC) was performed with an SDT Q600 (TA Instruments) calorimeter. Further details on the structural characterisation, including the techniques for the calculation of the number density and volume fraction of different phases were described in Ref. [18].

3. Results

3.1. Deformation structures

Cold rolling elongates the initial grains along the rolling direction (Fig. 2 in Ref. [3]). The cell structure and separate MBs evolve after a rolling reduction of 40% (ε ~0.51), while dense MBs appear after a rolling reduction of 60% (ε of ~0.92) [3]. Low-angle boundaries (LABs) transform into high-angle boundaries (HABs) with increasing rolling reduction. A lamellar structure with planar HABs and interboundary spacing of ~340 nm evolve after a reduction of 70% (ε~1.20) [3]. The lamellas are subdivided by transverse LABs which results in interboundary spacings of ~90 nm (Fig. 5 in Ref. [3]). The densities of the free lattice (so-called forest) dislocations are 8.4 × 10^{14}, 2 × 10^{15} and 4 × 10^{15} m^{-2} after rolling with reductions of 10%, 40% and 80%, respectively. Detailed description and TEM-micrographs of the deformed structures can be found in Ref. [3].

3.2. Mechanical properties

Cold rolling with reductions of 10%, 40% and 80% increases the microhardness from 96 ± 1 (after a solution treatment) to 130 ± 2, 164 ± 1 and 179 ± 2 $HV_{0.2}$, respectively [3]. The measured hardness of the cold rolled alloy in the course of ageing is displayed in Fig. 1. It is worth noting that the ageing curves of the alloy subjected to cold rolling with a reduction of 10% (Fig. 1) and tension with an engineering strain of ≤7% [18] show similar age hardening trends. Peak ageing with a hardness of 161 ± 2 $HV_{0.2}$ is attained after 2 h in the sample rolled with a reduction of 10%. Upon further ageing up to 10 h the hardness decreases to 157 ± 3 $HV_{0.2}$ indicating over-ageing. Therefore, the increase in the peak

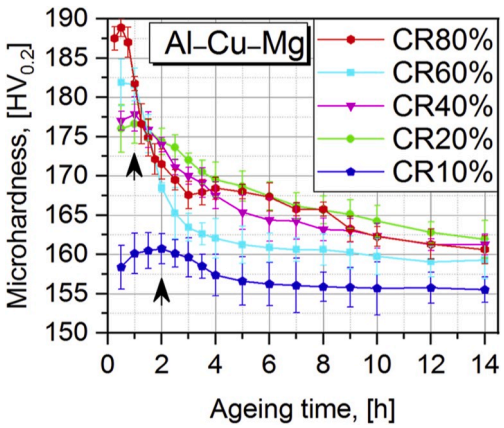

Fig. 1. Age hardening curves demonstrating evolution of AA2519 Vickers microhardness as a function of increasing pre-strain and ageing time at 190 °C. The black arrows denote the peak-ageing positions.

hardness is 23% which is lower than that of the non-deformed alloy; the hardness increases from 96 ± 1 to 150 ± 2 $HV_{0.2}$ (56%) [23].

On the other hand, the hardness measurements curves indicate that the age hardening of the material subjected to cold rolling with reductions of ≥20% occur in other way, namely softening follows a slight hardening after ~1 h. The subsequent increasing rolling reduction reduces the peak hardening and pronounces softening, whereas the hardness tends to increase with increasing level of pre-straining after rolling followed by ageing. Evidently, cold rolling with reduction of ≥40% suppresses peak ageing. At a reduction of 80%, the increase in the peak hardness is insignificant (10 ± 1 $HV_{0.2}$ or ~5%). The softening upon over-ageing increases from 6 ± 1 $HV_{0.2}$ (~4%) to 15 ± 2 $HV_{0.2}$ (~8%) and 26 ± 2 $HV_{0.2}$ (~14%) with increasing rolling reduction from 10% to 40% and 80%, respectively. After rolling with a reduction of 40%, softening occurs gradually up to 10 h, while in the material subjected to rolling with a reduction of ≥60%, a poorly defined plateau of approximately constant hardness is observed after 4 h.

Tensile tests were conducted to investigate the evolution of the mechanical performance of the alloy during ageing. Typical curves of the peak- and over-aged conditions are presented in Fig. 2. For the sake of brevity, the relevant main numerical results (σ_{YS}, σ_{UTS}, ε_U, δ, and σ_{YS}/σ_{UTS} ratio) are provided in the Supplementary Figs. S1 and S2. The shapes of the AA2519 σ–ε curves under peak-aged and cold-rolled [3] conditions are nearly the same. Pronounced strain hardening occurs after yielding up to the onset of necking. The work hardening, $d\sigma/d\varepsilon$, after yielding decreases insignificantly with increasing rolling reduction. At rolling reductions of 10% and 20%, peak ageing increases σ_{YS} and σ_{UTS} by ~10%. Peak ageing and the increase in the rolling reduction increase the σ_{YS}/σ_{UTS} value (Fig. S2). As expected, the increase in σ_{YS}/σ_{UTS} value attributed to work hardening correlates with the decrease in ductility (Fig. S1). At rolling reductions of ≥20%, the pre-strain seems to have no effect on the strain hardening behaviour. With increasing rolling reduction to 40%, the effect of peak ageing on the mechanical behaviour becomes insignificant, and at a rolling reduction of 80%, the σ–ε curves after rolling and further peak ageing are almost the same.

After over-ageing, extensive strain hardening occurs initially (Fig. 2c and d) with a well-defined peak in the flow stress. It is clearly seen that the shape of the σ–ε curves of the over-aged alloy depends on the rolling reduction. Increasing the pre-strain increases σ_{YS} and σ_{YS}/σ_{UTS} and decreases the elongation-to-failure (Figs. S1 and S2). As a result, the alloy subjected to rolling with a reduction of 10% exhibits higher σ_{UTS}, ε_U and δ_T and lower σ_{YS} in comparison with those of the alloy rolled with a reduction of 80%. The value of Tabor's constant (c) in relationship $\sigma_{UTS} = c \times HV$ [18,23,26,27] is different under the peak (~3.1) and over-ageing (~2.9) conditions. This fact is attributed to the different σ_{YS}/σ_{UTS} values (Fig. S2) [26].

3.3. DSC analysis

The DSC curve shapes exhibit insignificant differences after cold rolling with reductions of ≥10% (Fig. 3) and a pre-strain of 7% [18].

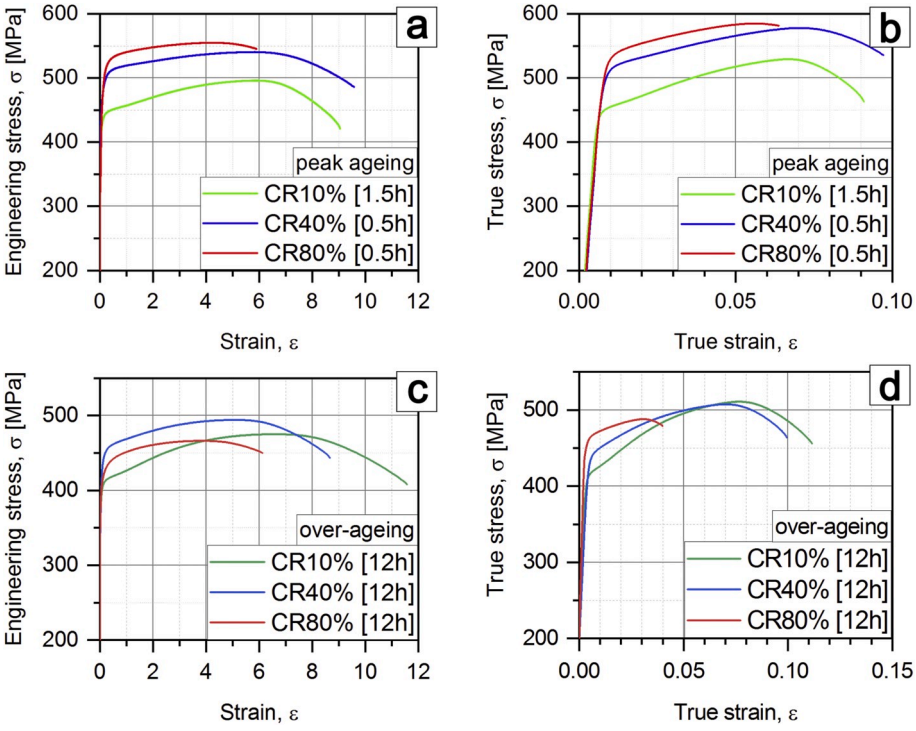

Fig. 2. Typical engineering stress–strain curves (a, c) and true stress–true strain curves (b, d) after peak ageing (a, b) and over-ageing (c, d). The numbers in square brackets indicate the ageing duration.

After extensive rolling an exothermic reaction associated with the simultaneous precipitation of the Ω- and θ′-phases is observed at 179 °C; in addition, an endothermic reaction associated with the onset of the dissolution of these phases and precipitation of the θ-phase occurs at 205 °C. There is no effect of strains ≥7% on the energy released with these reactions. Reviewing the aforementioned data, the increasing pre-strain shifts the precipitation of the Ω-, θ′- and θ-phases to lower temperatures [18,23].

3.4. Precipitation structures

To associate the observed mechanical properties with the evolution of the precipitation, systematic TEM investigations were conducted at different processing stages of the samples. Therefore, AA2519 alloy was aged to impart the underaged (Section 3.4.1), peak aged (Section 3.4.2) and over-aged conditions (Section 3.4.3).

3.4.1. Early stage of precipitates

The distributions of secondary-phase particles exhibit no differences after a pre-strain by 7% stretching [18] and cold rolling with a reduction of 10% followed by under-ageing (Fig. 4a-c). Discontinuous streaking through the $\{002\}_\alpha$ spots could be rarely observed (Fig. 4c), thereby indicating a low volume fraction of the θ″-phase in the material rolled with a reduction of 10% [1,18,23]. No solid evidence for the formation of Guinier–Preston (GP) zones was found. It was noticed that the θ′-phase tends to replace the θ″-phase with increasing rolling reduction. At an ε of ~0.11, the volume fractions of the θ″- and θ′-phases are nearly equal (Fig. 4a and b). The increasing pre-straining level decreases the θ″-phase volume fraction. It is obvious that after rolling with a strain of ~1.6 the θ′-phase is the dominant transition phase (Fig. 4d–f).

The selected area electron diffraction (SAED) patterns taken along the $<011>_\alpha$ zone axis show streaking along the $<111>_\alpha$ directions and distinct diffraction spots at $1/3<022>_\alpha$ and $2/3<022>_\alpha$ positions, thereby indicating the precipitation of thin Ω-phase plates on the $\{111\}_\alpha$ matrix planes (Fig. 5b and d) [1,18,23]. It is seen that the volume fraction of this phase is significantly higher than that after low pre-straining [18]. After rolling with a reduction of 80% the precipitation of the Ω-phase occured rarely after a very short ageing time (for 15 min). It should be emphasized that most precipitates with $\{111\}_\alpha$ habit plane belong to the so-called "Ω_{II}-type", i.e. were nucleated on the θ′-phase/Al interfaces [18]. Homogeneously nucleated particles of the Ω_I-phase were rarely observed after rolling with a reduction of 10% and are not present after rolling with a reduction of 80%. Therefore, intense

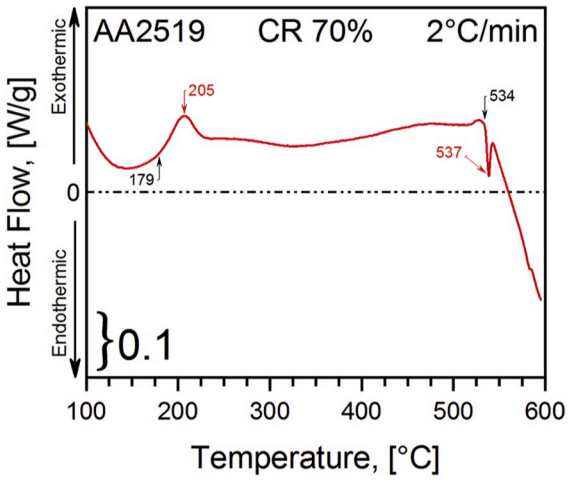

Fig. 3. DSC thermograms of cold-rolled AA2519. The black and red arrows indicate the onset of a reaction and peak temperatures, respectively. (For interpretation of the references to colour in this figure legend, the reader is referred to the Web version of this article.)

pre-straining suppresses the formation of a uniformly nucleated θ″-phase and promotes the precipitation of the θ′-phase and Ω_{II}-platelets. This is provided by the increased number of dislocations, which functions as nucleation sites for the θ′-phase and, hence, for the Ω_{II}-phase [18].

3.4.2. Fully age-hardened microstructure

Under peak ageing with a pre-strain of ≥0.11 the θ′-phase replaces the θ″-phase completely (Fig. 6). It is worth noting that after rolling with an ε ~0.11 and tensioning with an ε ~0.07 followed by peak ageing the dimensions of the θ′-phase platelets are nearly equal and significantly smaller than those without pre-strain (Table 1) [18,23]. Furthermore, the number density is higher by a factor of two, and the volume fractions are higher by 50% [18]. At $\varepsilon \geq 0.51$, the increasing rolling reduction leads to a refinement of the θ′-phase; it decreases its volume fraction and increases its number density (Fig. 6, Table 1). Herewith, the aspect ratio (AR, diameter-to-thickness ratio) of the θ′-phase, which is crucial for effective strengthening, is virtually independent of the rolling reduction (Table 1).

Distinct diffusive streaks through $\{111\}_\alpha$ and distinct diffraction spots at $1/3<022>_\alpha$ and $2/3<022>_\alpha$ positions can be clearly observed in the SAED pattern taken along $<011>_\alpha$ zone axis (Fig. 7). This indicates unambiguously the Ω-phase precipitation [18,23]. The dimensions of the Ω-phase after rolling with an ε of ~0.11 and tensioning with an ε of ~0.07 followed by peak-ageing are essentially equal, whereas the volume fraction and number density after cold rolling are remarkably lower than those after tensioning (Table 2) [18,23,26]. The number density of the Ω-phase increases by a factor of ~5 with increasing rolling reduction from 10% to 80% (Fig. 7, Table 2). This increase is attributed to an increase in the volume fraction by 60% and a decrease in the plate diameter by 35%. The thickness of the Ω-phase plates is nearly independent of the rolling reduction. A major portion of the Ω-phase nucleates at the edges of the θ′-phase, while some platelets of this phase nucleate homogeneously. In contrast to those of the deformed *via* stretching [18,26] the dimensions of the Ω_{II} and the Ω_I-phases are nearly equal. Thus, cold rolling followed by peak ageing provides the formation of a dense network of platelets on $\{100\}_\alpha$ and $\{111\}_\alpha$ planes. The number density of the Ω-phase tends to approach the number density of the θ′-phase with increasing rolling reduction. Thus, increasing rolling reductions refine both type of particles with $\{100\}_\alpha$ and $\{111\}_\alpha$ habit planes.

In addition to the main strengthening precipitates, a fairly small amount of θ_{II}'-phase with $\{110\}_\alpha$ habit plane (Fig. 7a) [18,28] was also found after rolling with a reduction of 10%. It is impossible to assert unequivocally that the nucleation of above phase is related to the pre-deformation. Simultaneously, the increasing rolling reduction suppresses the precipitation of this phase. The striking feature of peak ageing after cold rolling with $\varepsilon \geq 0.51$ is a copious precipitation of the θ-phase and coarse particles of the θ′-phase on the HABs and LABs, respectively (Fig. 8). The boundary precipitations of the θ-phase exhibit irregular shapes with longitudinal dimensions ranging from 50 to 200 nm. It is worth noting that the shapes of these θ-phase particles and boundary particles evolved during natural ageing of Al–4wt.%Cu alloy subjected to intense plastic straining at room temperature [24] are nearly equal and bigger than the θ-phase particles precipitated homogeneously and having plate-like shapes in Al–3.4wt.%Cu alloy after ageing at 190 °C without pre-straining [29]. The average diameter and thickness of the θ′-phase platelets nucleated on LABs are ~50 and ~10 nm, respectively. These are higher by factors 2 and 4 than the dimensions of the phase precipitated on the free dislocations (Table 1). The θ′-phase particles located on LABs retain their orientation relationship with the Al matrix. It is worth noting that the θ′-phase dispersoids located on the dislocations comprising the LABs loose a part of a coherency of its interfaces owing to the interactions with dislocations belonging to two or more slip systems. This results in the extensive coarsening of these particles [22] and the formation of θ′-phase chains

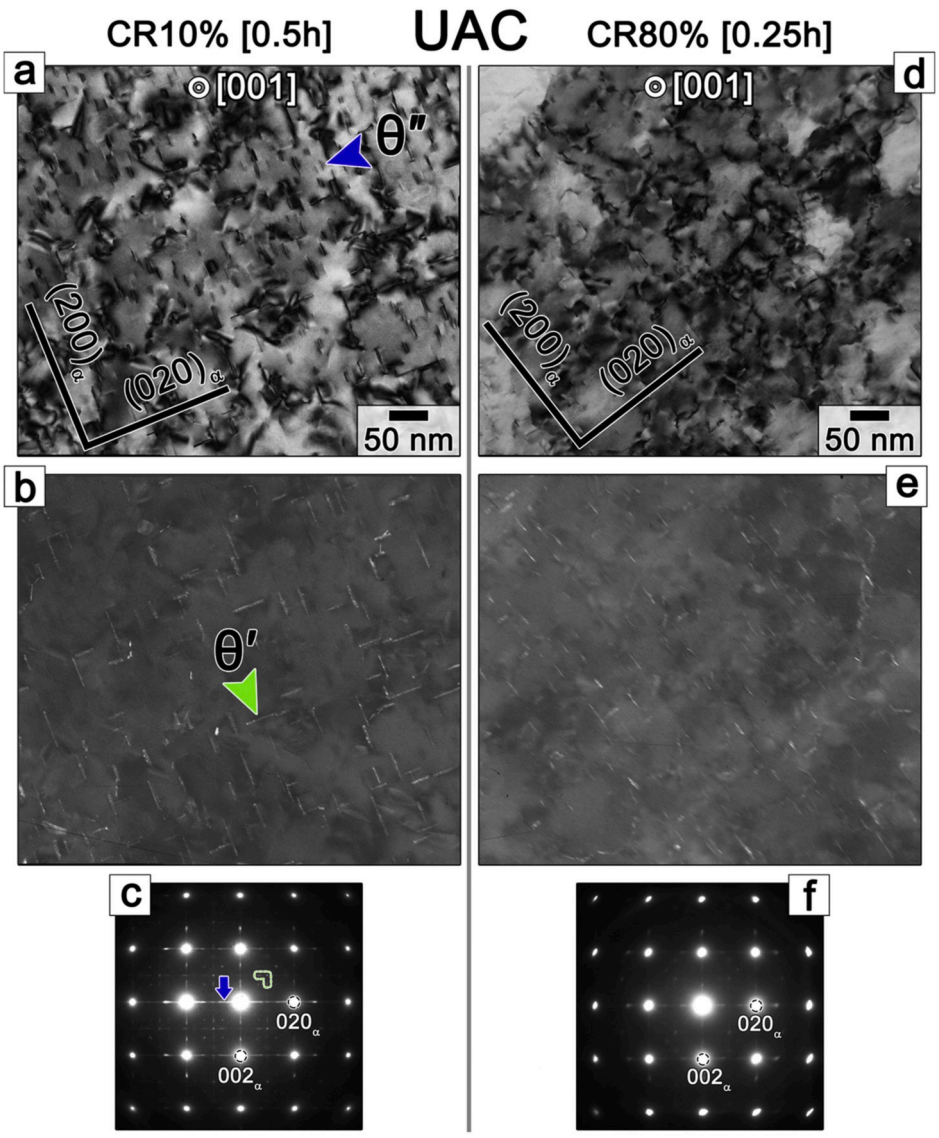

Fig. 4. Representative BF-TEM (a, d) and corresponding DF-TEM (b, e) micrographs taken using the $\{011\}_{Al}$ reflection corresponds to the same regions in (a, d). The images demonstrate the abundant presence of θ″ and θ′ precipitates in AA2519 after cold rolling followed by under-ageing. Because the *c* parameter of θ″ differs from those of aluminium, the aluminium planes parallel to the plate are distorted by elastic coherency strains (clearly visible in a). The SAED patterns (c, f) contain spots at $\{110\}_{\alpha}$ positions (green figure) and week streaks (blue arrow), which can be attributed to the θ′-phase and to θ″-phases, respectively. Schematic SAED patterns were presented in previous works [2,18,26]. (For interpretation of the references to colour in this figure legend, the reader is referred to the Web version of this article.)

along the LABs (Fig. 8d). The difference between the θ′-phase nucleated on the free dislocations and LABs consists in their thicknesses and aspect ratios. As a result, their contributions to the overall strength are substantially different.

3.4.3. *Over-ageing*

Increasing the ageing duration strongly affects the morphological characteristics of secondary phase particles (Figs. 9 and 10, Tables 1 and 2). Over-ageing after rolling with a reduction of 10% is attributed to the thickening of the θ′-phase by consuming Cu from Al matrix. This increases the volume fraction by +45% and the number density of this reinforcement phase decreases insignificantly (Fig. 9, Table 1). As a result, a dense network of a relatively thick θ′-phase remains and the softening is slight.

Semi-continuous chains of θ′ - and θ-phases appear on the LABs and HABs, respectively, after rolling with a reduction of 80% followed by over-ageing (Fig. 9c). The platelets diameter, AR, and number density are insignificantly smaller than these values after a rolling reduction of 10%, while the volume fraction of the θ′-phase is ~60% lower (Table 1). Moreover, a high portion of the θ′-phase located on the LABs does not contribute to the overall strength. Thus, the extensive softening during over-ageing is attributed to the dramatic decrease in the volume fraction of the matrix θ′-phase and decreasing AR of its particles [23,30].

Over-ageing leads to concurrent coarsening and dissolution of the Ω-phase (Fig. 10 and Table 2). During over-ageing after rolling with reductions of 10% and 80%, the number densities of the Ω-phase decrease by factors of 4 and 10 and the volume fraction decreases by 50 and 60%, respectively. The thickness of the Ω-phase after rolling with a reduction of 10% is nearly independent of the ageing duration whereas the diameter increases by 10%. By contrast, after rolling with a reduction of 80% the thickness and diameter increase by 40% and 50%, respectively. The Ω-phase AR decreases by ~26%.

Thus, over-ageing strongly diminishes the strengthening efficiency of the θ′- and Ω-phases. The main difference between the low and high prestrains is the precipitation and growth of a thermodynamically stable θ-phase at the HABs at the expense of the metastable θ′- and Ω-phases. Consequently, after rolling with a reduction of 80% followed by over-ageing, the overall volume fraction of these two phases, which are effective strengthening agents [18,23,30,31], is by a factor of 2 lower than that after rolling with a reduction of 10%. The precipitation of boundary particles resulting in dissolution of matrix θ′- and Ω-phases in accordance with the Gibbs-Thomson schema [18,22] promotes softening under over-ageing.

The data of EBSD analysis (not presented here) show no ageing effect

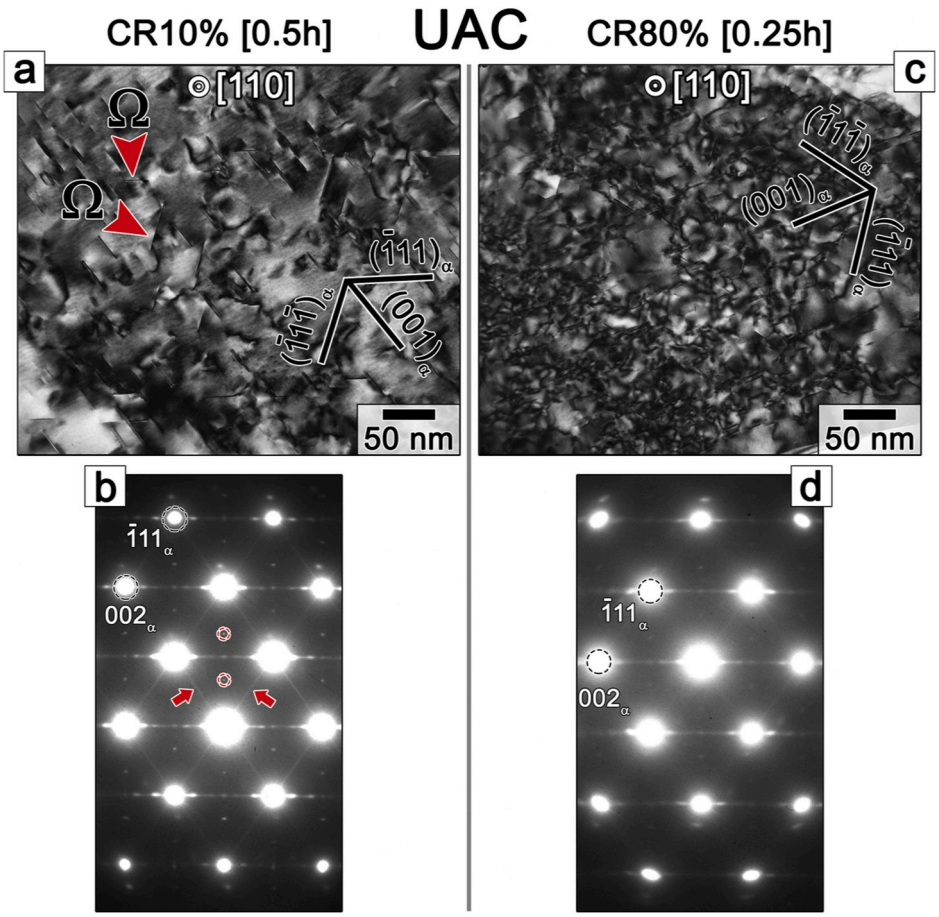

Fig. 5. BF-TEM images and corresponding SAED patterns showing the plenty of edgewise Ω (lying on the $\{111\}_\alpha$) and θ″/θ′ (lying on the $\{100\}_\alpha$) plates of the under-age cold rolled AA2519. The observations illustrate the presence of two variants of the plate-shaped precipitates lying on the $\{111\}_\alpha$ planes of the matrix (red arrows). The streaking along $\{111\}_\alpha$ (red arrows) and diffraction spots at 1/3 and 2/3 $[220]_\alpha$ (red circles) associated with Ω precipitation in the SAED patterns are evident. (For interpretation of the references to colour in this figure legend, the reader is referred to the Web version of this article.)

on the grain dimensions. The strain-induced LABs and HABs are retained during ageing at 190 °C for any duration. The TEM observations without objective aperture and weak-beam dark-field technique indicate a decrease in the dislocation density during ageing after rolling with reductions ≥40%, i.e. a recovery takes place. The effect of the under-ageing on the mechanical properties (Fig. S1) supports this conclusion. At rolling reductions ≥40%, the ductility and uniform elongation increase owing to the decreasing σ_{YS}/σ_{UTS}. So, we may assume that the recovery promotes strain hardening under tension. Our findings are broadly in line with the observations of Starink et al. [6].

4. Discussion

4.1. Effect of rolling on precipitation sequence

At 190 °C, the decomposition of the SSSS in the AA2519 alloy tensioned with true strains ranging from 0.03 to 0.07 and cold rolled at ε < 0.51 proceeds *via* two independent precipitation sequences [18,23]:

$$\text{SSSS} \rightarrow \text{GP zones} \rightarrow \theta'' \text{-phase} \rightarrow \theta' \text{-phase} + \Omega_{II} \text{-phase} \rightarrow \theta' \text{-phase} \rightarrow \theta \text{-phase} \quad (2)$$

$$\text{SSSS} \rightarrow \{111\} \text{ clusters} \rightarrow \Omega_I \text{-phase} \rightarrow \theta \text{-phase} \quad (3)$$

An increasing pre-strain intensifies the precipitation sequence (2) and prevents the reaction (3). At $\varepsilon \geq 0.51$, the precipitation sequence (2) converts into the following one:

$$\text{SSSS} \rightarrow \theta' \text{-phase} + \Omega_{II} \text{-phase} \rightarrow \theta' \text{-phase} \rightarrow \theta \text{-phase} \quad (4)$$

It is known [31] that a dislocation causes an elastic distortion in crystalline lattice around the defect line. The interaction between this stress field and the undersized substitutional solutes (e.g. Cu) leads to the migration of these atoms towards the compressed regions above the slip plane. This stress-induced migration leads to the formation of Cottrell atmospheres [31]. Dislocations gliding during cold rolling and a decrease in the dislocation spacing from 34.5 nm at ε of ~0.11 to 15.8 nm at ε of ~1.61 promote the formation of these Cottrell atmospheres which leads to two consequences. First, the homogeneous nucleation of the GP-zones and θ″-phase is suppressed owing to the trapping of a number of Cu atoms by dislocations. Second, the Cottrell atmospheres function as nuclei for the θ′-phase plates and, therefore, the precipitation of the θ′-phase on dislocations becomes strongly feasible due to the decreased activation barrier [22,32].

Furthermore, Cu segregations appear on the strain-induced boundaries by a depletion of this element around these boundaries [25,33,34]; this induces an additional precipitation sequence:

$$\text{SSSS} \rightarrow \text{boundary segregation of Cu} \rightarrow \text{boundary } \theta\text{-phase} \quad (5)$$

During extensive cold rolling, the forced migration of strain-induced boundaries collecting Cu atoms from the swept matrix results in the segregation of Cu atoms along them [25,33,34]. The strain-induced HABs (often called "non-equilibrium") contain high density of lattice dislocations [35], which also promote the segregation of Cu atoms on them [36]. Therefore, the formation of a boundary θ-phase occurs owing to the superposition of two factors. First, a fast diffusion path for Cu atoms along these boundaries, because the diffusional grain boundary width is significantly larger than that of the HABs containing low density of grain boundary dislocations [34,37]. Second, HABs containing a high density of grain boundary dislocations can accommodate more solute elements than annealed boundaries and, therefore, the Cu solute excess around the boundaries increases, decreasing the activation barrier for nucleation of the stable θ-phase [34]. It is worth noting that in contrast

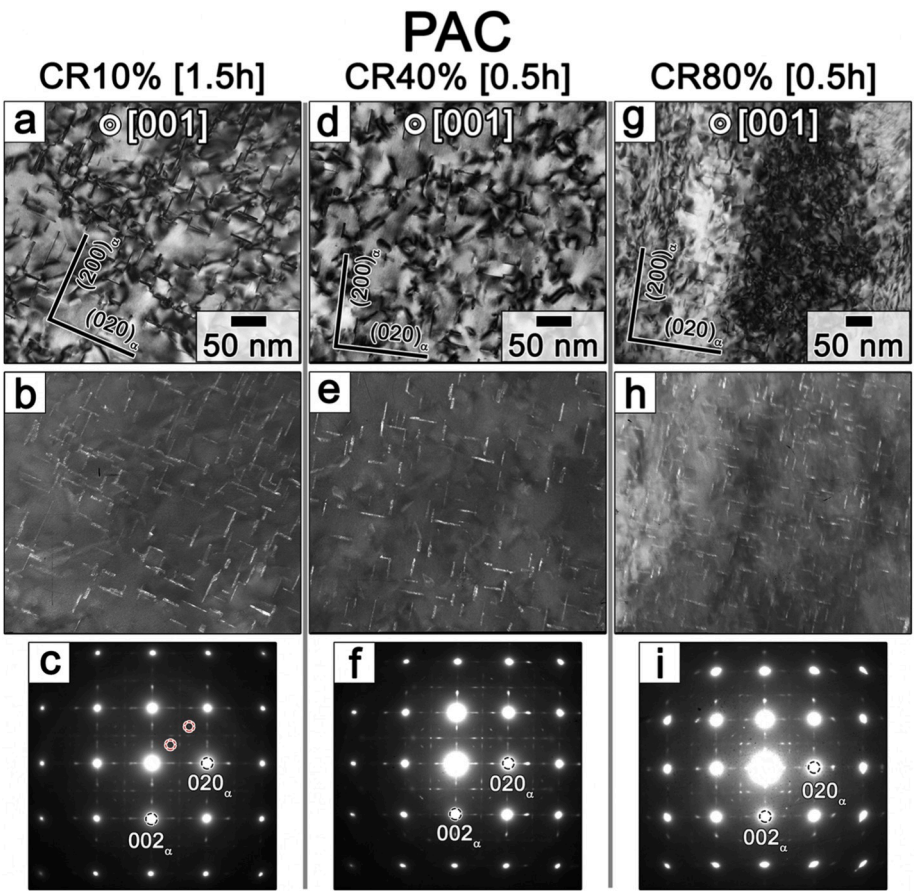

Fig. 6. Intragranular precipitation of metastable phases in peak aged AA2519. A set of four spots that are characteristic for the Ω reflections (marked by red circles) from four $\{111\}_\alpha$ habit plane variants, are symmetrically opposed on the diagonals surrounding the 011_{Al} position at 1/3 and 2/3$\{011\}_\alpha$. DF-TEM (b, e, f) taken using the $\{011\}_{Al}$ reflection corresponds to the same regions in (a, d, g). The intensity asymmetry of the matrix spots reflects the presence of long-range stresses in the matrix.

Table 1
Effect of pre-strain and ageing conditions on geometric dimensions, number density and volume fraction of θ′-phase. Data for T6 treatment [23] and tensile pre-strain [18] are presented for comparison.

Temper	Pre strain, %	Condition	Aging time, h	Mean plate dimensions, nm		Aspect ratio	Number density × 10^{20}, #/m^{-3}	Volume fraction, %	σ_{YS}, MPa
				Diameter	Thickness				
T6	0	PAC	12	132 ± 77	4.5 ± 1	30	4 ± 0.3	2.4 ± 0.9	292 ± 1
T8	Tensile 3%	PAC	2	49 ± 23	3 ± 0.8	16	28 ± 0.8	1.7 ± 0.2	395 ± 3
	7%	PAC	1.5	35 ± 17	3 ± 0.9	12	60 ± 0.7	2 ± 0.6	421 ± 1
		OAC	12	34 ± 14	3.3 ± 1	10	57 ± 0.1	2 ± 0.1	380 ± 2
	Rolling 10%	PAC	1.5	38 ± 13	3.2 ± 0.90	10	114 ± 18	3 ± 0.9	441 ± 4
		OAC	12	36 ± 15	4 ± 1	9	91 ± 17	4.4 ± 0.2	411 ± 2
	80%	PAC	0.5	23 ± 8	2.5 ± 0.7	10	141 ± 24	1.7 ± 0.3	509 ± 1
		OAC	12	26 ± 8	3.5 ± 1	7.5	85 ± 10	1.9 ± 0.2	428 ± 3

Table 2
Effect of pre-strain and ageing conditions on geometric dimensions, number density and volume fraction of Ω-phase. Data for T6 treatment [23] and tensile pre-strain [18] are presented for comparison.

Temper	Pre strain, %	Condition	Aging time,h	Mean plate dimensions, nm		Aspect ratio	Number density × 10^{20}, #/m^{-3}	Volume fraction, %
				Diameter	Thickness			
T6	0	UAC	0.5	26 ± 12	0.8 ± 0.1	33	–	–
		PAC #2	12	117 ± 68	1 ± 0.2	120	1.2 ± 1.8*	0.08 ± 0.07
T8	Tensile 1	UAC	0.5	33 ± 12	0.85 ± 0.20	39	6 ± 3.6	0.03 ± 0.01
		PAC #1	2.5	47 ± 24	0.8 ± 0.2	58	4 ± 3	0.06 ± 0.04
		PAC #2	12	141 ± 81	1.2 ± 0.3	119	0.5 ± 0.3	0.08 ± 0.02
	3	UAC	0.5	36 ± 12	0.8 ± 0.2	47	5 ± 1.7	0.04 ± 0.01
		PAC	2	44 ± 20	1 ± 0.3	46	11 ± 4	0.14 ± 0.05
	7	UAC	0.5	34 ± 13	0.8 ± 0.2	40	16 ± 0.3	0.11 ± 0.04
		PAC	1.5	40 ± 18	1.1 ± 0.3	37	23 ± 10	0.3 ± 0.1
	Rolling 10%	PAC	1.5	40 ± 17	1.1 ± 0.3	37	14 ± 4	0.17 ± 0.05
		OAC	12	44 ± 18	1.6 ± 0.4	28	3.6 ± 1.3	0.09 ± 0.06
	80%	PAC	0.5	23 ± 8	1 ± 0.24	24	73 ± 11	0.27 ± 0.05
		OAC	12	32 ± 11	1.9 ± 0.6	18	7.4 ± 2.8	0.11 ± 0.04

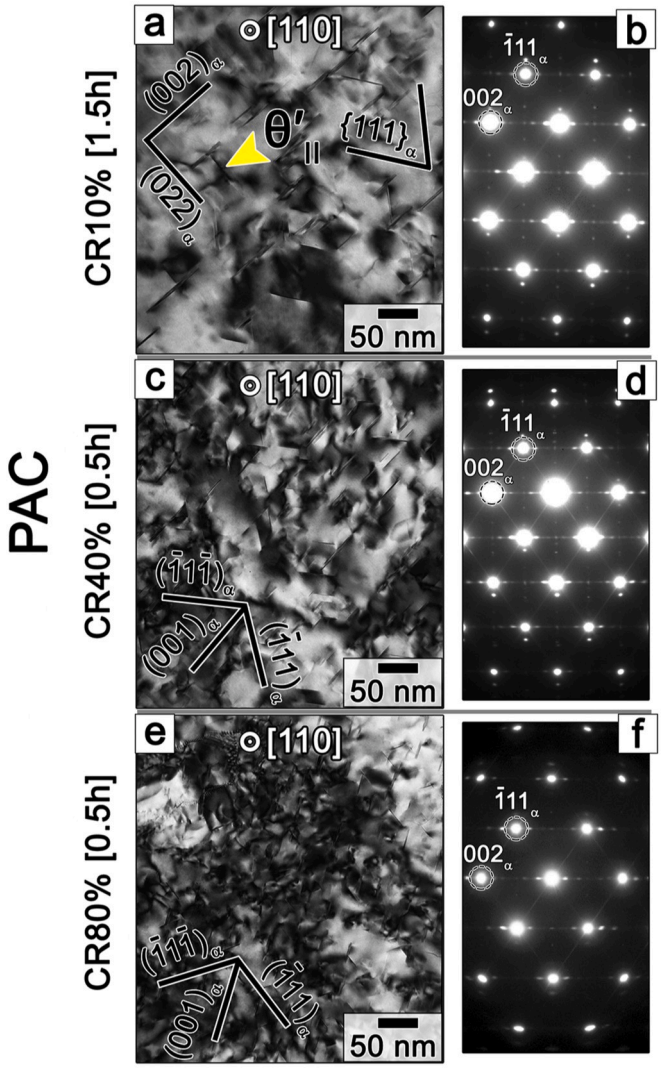

Fig. 7. BF-TEM micrograph and corresponding SAED patterns recorded near the $<011>_{\alpha}$ orientation after rolling and peak ageing.

to the intense plastic straining [24,38], the precipitation of the θ-phase was detected at a relatively high temperature (190 °C). Therefore, an increasing strain that increases the density of the strain-induced boundaries strongly promotes the formation of a θ-phase which may appear even after a long-term natural ageing [24,25].

The number density of the Ω-phase increases by a factor of ~4 with increasing pre-strain from 0.11 to 1.61 despite the increase in the number density of the θ′-phase (i.e. nucleation sites for the Ω_{II}-phase) by 30%. It is apparent that the increased lattice dislocations promotes the segregation of Mg atoms on the semi-coherent θ′-phase/Al matrix interfaces [18,39,40], which facilitates the nucleation of the Ω_{II}-phase.

4.2. Effect of rolling reduction on mechanical properties

The experimental data show that the two factors unveiled in Section 1 are responsible for diminishing the age-hardening phenomenon in the AA2519 alloy with increasing pre-strain. First, the pre-strain affects the distribution of secondary-phase particles. The character of this effect depends on the formation of strain-induced boundaries. At $\varepsilon < 0.51$, no boundaries evolve during rolling and increasing the pre-strain followed by under-ageing leads to a replacement of the θ″-phase by a θ′-phase (see Sections 3.4.2 and 4.1). Peak artificial ageing after cold rolling with a reduction of 10% (ε ~0.11) provides an increment in σ_{YS} of 100 MPa. This is slightly higher compared with an increase (85 MPa) in the yield stress of AA2519 which was stretched with ε of ~0.07 followed by peak aging [18]. This observation may be ascribed to the increased number density, volume fraction and distribution uniformity of the θ′-phase. The contribution of the Ω_{II}-phase to overall σ_{YS} increases with increasing pre-strain imposed by the cold rolling procedure before peak ageing due to the increasing number density of the semi-coherent θ′-phase/Al matrix interfaces, which serve as nucleation sites. Over-ageing is relevant to coarsening behaviour of the θ′- and Ω-phases and the dissolution of the Ω_{II}-phase (Section 3.4.3). As a result, at an ε ~0.07 [18], σ_{YS} decreases insignificantly (by approximately 10 MPa), and at an ε ~0.51, a high decrease of ~48 MPa occurs. At $\varepsilon \geq 0.51$, the formation of strain-induced boundaries with low- or high-misorientation strongly increases the number of nucleation sites for the coarse θ′- and θ-phases, respectively. These boundary particles contribute little or not at all to the overall strength and consume significant portions of Cu solutes, which is the required element for a θ′-phase formation. Consequently, the volume fraction of θ′-phase nucleated on free dislocations in the Al matrix decreases with pre-straining. The decreasing number of key strengthening agents decreases the peak age-hardening with increasing pre-strain.

Second, the superposition of long-range elastic strain fields originating from dislocations and the θ′-phase nucleated on these dislocations decreases the increase in σ_{YS} under peak ageing. The lattice dislocations facilitate the formation of θ′-phase plates with minimal volume and shape changes because the elastic strain energy plays a dominant role compared with the interface energies in the nucleation [40,41]. The independence of the θ′-phase AR from the pre-strain indicates that the pre-strain has no effect on the basic mechanisms that control the nucleation of this phase [41,42]. The superposition of the long-stress fields originated from the dislocations, θ′-phase plates and the Ω_{II}-phase reduces the overall elastic strain under peak ageing. As a result, the increase in σ_{YS} is due to the decreased peak ageing (46 MPa) at an ε of ~0.51. In addition, the internal elastic stress fields affect the growth mechanism strongly [41,42]. As a result, the θ′-phase growth depends on the dislocation density. An increased dislocation density restricts the θ′-phase growth owing to the interaction between the coherent stresses originating from the θ′-phase plates [43] and stress fields originating from the dislocations [39]. The strain field of a dislocation can reduce the misfit of the θ′-phase interfaces in two <100> matrix directions [22]. The θ′-phase has a positive vacancy in character misfit (42.4% along the *c*-direction) and its formation below a dislocation strongly reduces the elastic strains [22,40]. It was assumed that the θ′-phase is non-shearable [1,22,23,30]. Therefore, the reduction in the misfit strain originates from this phase decreases the efficiency of the strengthening agent. Table 1 and the data in Refs. [18,23] indicate unambiguously that the refinement of the θ′-phase contributes to a decreasing peak age-hardening. Under over-ageing, the growth of the θ′-phase occurs by thickening, which is unusual [40,42]. The coarsening of the θ′-phase under over-ageing leads to loss of coherency of its broad interfaces, whereas the edges of the plates of this phase become incoherent [22]. Moreover, the strengthening efficiency of this particle decreases owing to a decreasing misfit strain, which provides a significant contribution to the extensive softening behaviour at $\varepsilon \geq 0.51$ [30,41].

The AR is a key parameter of the strengthening efficiency of the shearable Ω-phase plates [41–47]. A decreasing AR with increasing rolling reduction decreases the strengthening efficiency of this phase [1, 30]. This decrease may be compensated by a strong increase in the number density of the Ω_{II}-phase nucleated on the θ′-phase/Al interfaces (Table 2) under peak ageing (Table 2). It is worth noting that at $\varepsilon > 0.51$, the loss of such an effective strengthening agent as θ′-phase cannot be compensated by the increased number density of the Ω-phase. Furthermore, the increasing pre-strain strongly facilitates the dissolution of the Ω_{II}-phase under over-ageing, which causes extensive softening.

In addition, it is most likely that the dislocation recovery of the rolled

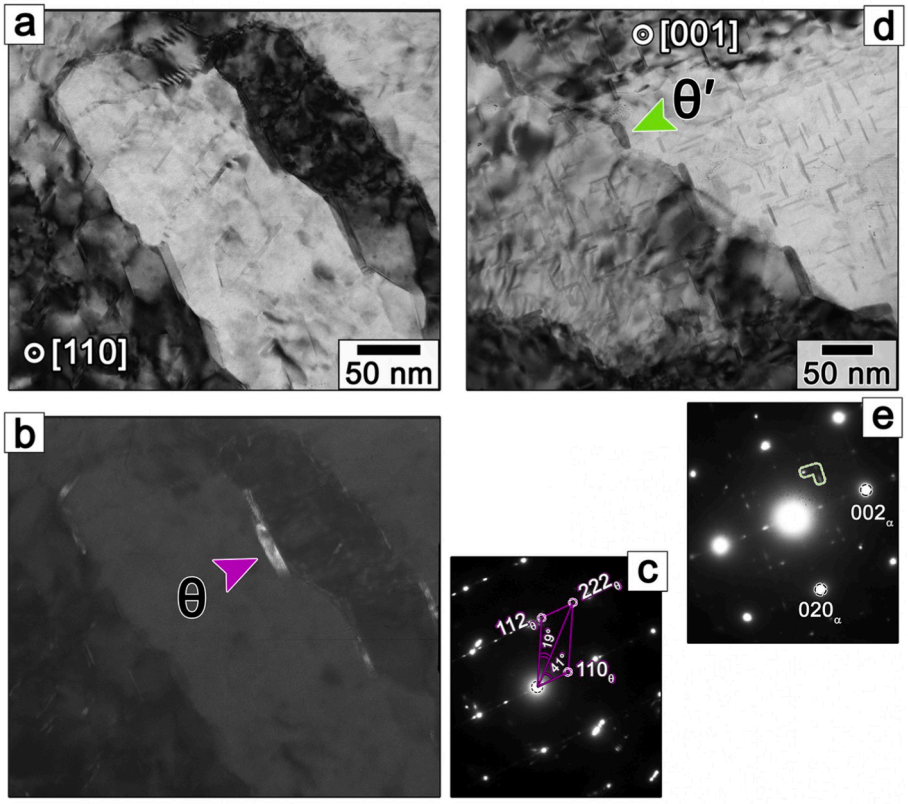

Fig. 8. Microstructure of AA2519 after rolling with reduction of 80% followed by ageing for 0.5 h. The images clearly demonstrate the precipitation of θ on the HABs and θ′ chain on the LABs. The DF-TEM image (b) was recorded using reflexes from θ. The EDXS point analysis (not shown here) of the phase point out that Al/Cu ratio of the precipitates is close to 2:1, i.e. the stoichiometry is Al_2Cu. The SAED pattern (e) includes only fundamental reflections from α-Al and spots specific to θ′ and Ω [18,23].

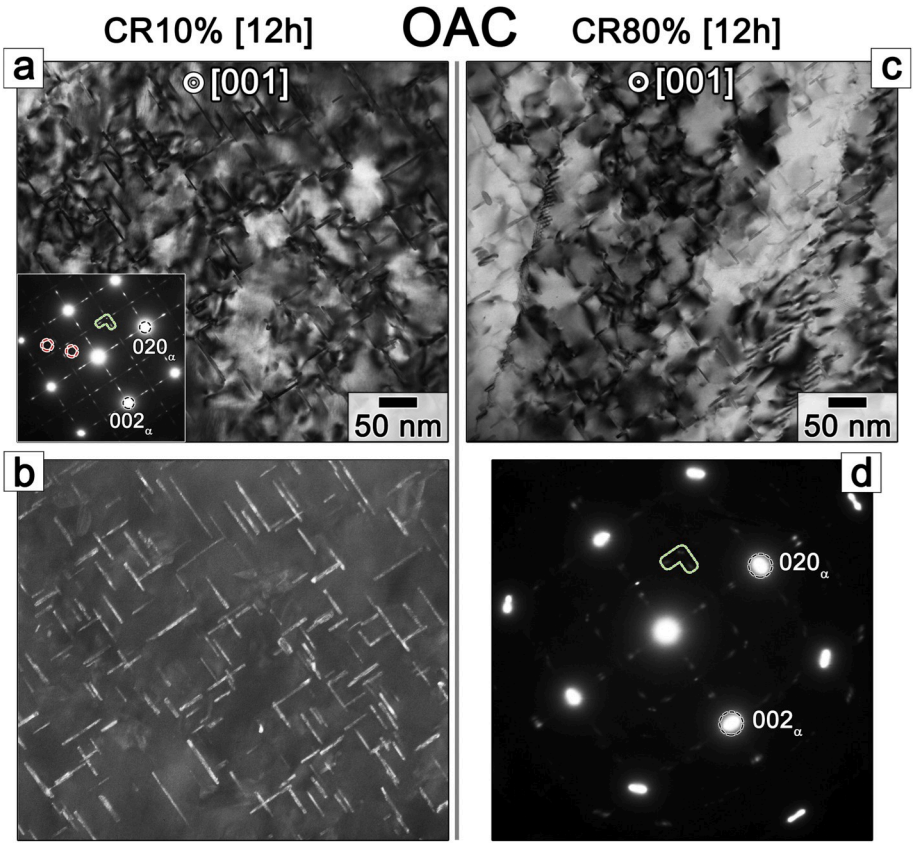

Fig. 9. TEM-micrographs and corresponding SAED patterns of AA2519 after cold rolling and over-ageing. DF-image (b) taken using the $\{011\}_{Al}$ reflection corresponds to the same region at those in (a). The diffraction spots at 1/3 and 2/3 $[220]_{\alpha}$ associated with Ω precipitation in the SAED patterns are evident after cold rolling with a reduction of 10% (red circles in inset), whereas they are very faint or practically absent in the 80% cold rolled sample (d). (For interpretation of the references to colour in this figure legend, the reader is referred to the Web version of this article.)

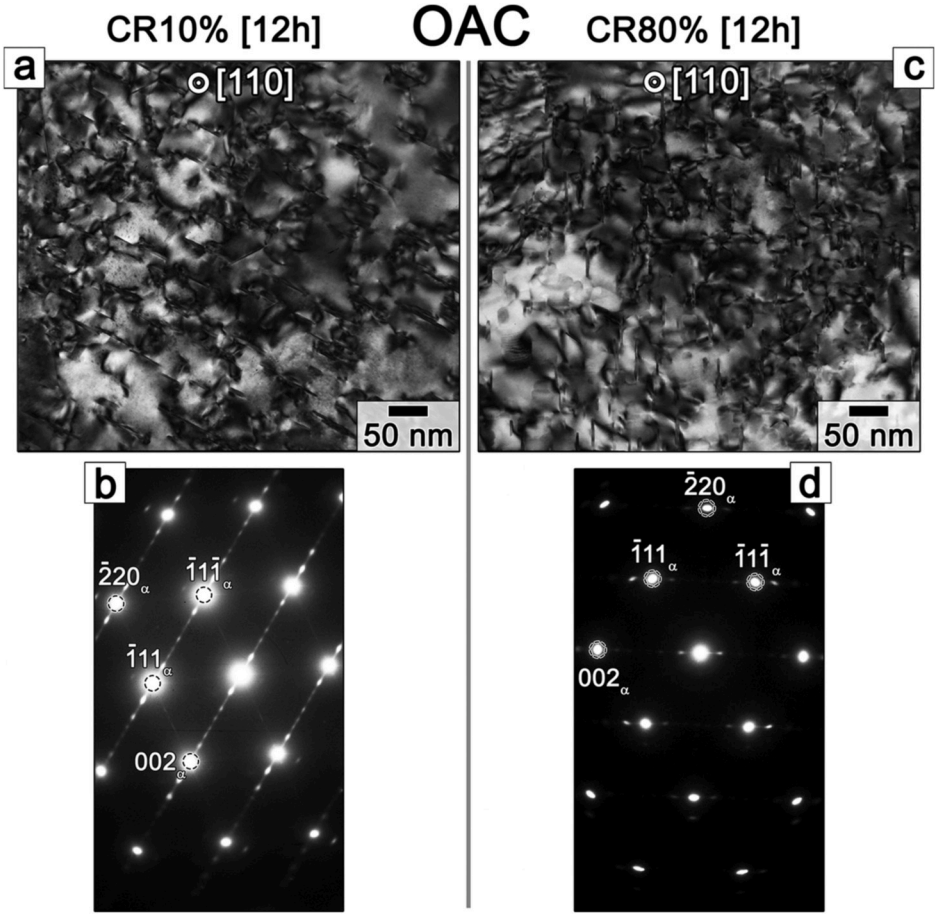

Fig. 10. BF-TEM micrographs (a, c) taken with $<011>_\alpha$ zone axes and SAED (b, d) after rolling with reductions of 10% (a, b) and 80% (c, d) followed by over-ageing for 12 h.

alloy during annealing at a relatively high temperature contributes to the weak age-hardening.

5. Conclusions

The mechanical properties and precipitation behaviour of AA2519 Al subjected to extensive cold rolling were examined during ageing at 190 °C. The major results are as follows:

1. Two different strain intervals could be distinguished based on the ageing behaviour. The following precipitation sequences occur at pre-strains ranging from 0.11 to 0.51:

SSSS → GP zones → θ″-phase → θ′-phase+Ω_{II}-phase → θ′-phase → θ-phase

SSSS → {111} clusters → Ω_I-phase → θ-phase

Increasing the pre-strain from 0.11 to 0.51 suppresses the precipitation of the Ω_I-phase and promotes the precipitation of the Ω_{II}-phase and its subsequent dissolution.

2. At pre-strains ranging from 0.51 to 1.61, an additional precipitation sequence appears:

SSSS → boundary segregation of Cu → boundary θ-phase

In addition, the precipitation of the θ″-phase is suppressed even during under-ageing. The following precipitation sequence occurs:

SSSS →θ′-phase+Ω_{II}-phase→θ′-phase→θ-phase

3. The peak age-hardening effect weakens with increasing pre-strain. The replacement of the θ″-phase by a θ′-phase and the effect of the pre-strain on the dimensions and shapes of θ′- and Ω-phases decrease σ_{YS} from 100 to 46 MPa with increasing pre-strain from 0.11 to 0.51. At $\varepsilon > 0.51$, the boundary precipitation of the θ-phase and the formation of θ′-phase chains on LABs strongly lead to a significant reduction in the volume fraction of the θ′-phase nucleated on free dislocations. These processes are responsible for the disappearance of the peak age-hardening. Moreover, the softening under over-ageing is relevant to the Ω_{II}-phase dissolution, θ′-phase coarsening and recovery phenomenon.

Data availability

The raw/processed data required to reproduce these findings cannot be shared at this time as the data also forms part of an ongoing study.

Declaration of competing interest

The authors declare that they have no known competing financial interests or personal relationships that could have appeared to influence the work reported in this paper.

CRediT authorship contribution statement

Ivan S. Zuiko: Conceptualization, Methodology, Investigation, Formal analysis, Writing - original draft, Visualization. **Rustam Kaibyshev:** Resources, Writing - review & editing, Supervision, Funding acquisition.

Acknowledgments

This work is financially supported by the Russian Science Foundation under Grant № 19-79-00304. The authors are grateful to the staff of the Joint Research Center, "Technology and Materials", Belgorod State National Research University for their assistance in the mechanical and structural characterisations. I.Z. wishes to thank V. Torganchuk for the assistance during the rolling procedure. The authors acknowledge Dr. S. Mironov and Dr. A. Belyakov for the primary reviews of the paper.

Appendix A. Supplementary data

Supplementary data to this article can be found online at https://doi.org/10.1016/j.msea.2020.139148.

References

[1] I. Palmer, D. St John, J.-F. Nie, M. Qian, Light Alloys: Metallurgy of the Light Metals, fifth ed., Butterworth-Heinemann, 2017.
[2] I.S. Zuiko, M.R. Gazizov, R.O. Kaibyshev, Effect of thermomechanical treatment on the microstructure, phase composition, and mechanical properties of Al–Cu–Mn–Mg–Zr alloy, Phys. Met. Metallogr. 117 (2016) 906–919, https://doi.org/10.1134/S0031918X16090088.
[3] I. Zuiko, R. Kaibyshev, Deformation structures and strengthening mechanisms in an Al–Cu alloy subjected to extensive cold rolling, Mater. Sci. Eng. A 702 (2017) 53–64, https://doi.org/10.1016/j.msea.2017.07.001.
[4] S. Malopheyev, V. Kulitskiy, R. Kaibyshev, Deformation structures and strengthening mechanisms in an Al–Mg–Sc–Zr alloy, J. Alloys Compd. 698 (2017) 957–966, https://doi.org/10.1016/j.jallcom.2016.12.289.
[5] I. Sabirov, M.Yu Murashkin, R.Z. Valiev, Nanostructured aluminium alloys produced by severe plastic deformation: new horizons in development, Mater. Sci. Eng. A 560 (2013) 1–24, https://doi.org/10.1016/j.msea.2012.09.020.
[6] Y. Chen, N. Gao, G. Sha, S.P. Ringer, M.J. Starink, Microstructural evolution, strengthening and thermal stability of an ultrafine-grained Al–Cu–Mg alloy, Acta Mater. 109 (2016) 202–212, https://doi.org/10.1016/j.actamat.2016.02.050.
[7] I.F. Mohamed, Y. Yonenaga, S. Lee, K. Edalati, Z. Horita, Age hardening and thermal stability of Al–Cu alloy processed by high-pressure torsion, Mater. Sci. Eng. A 627 (2015) 111–118, https://doi.org/10.1016/j.msea.2014.12.117.
[8] P.P. Ma, C.H. Liu, C.L. Wu, L.M. Liu, J.H. Chen, Mechanical properties enhanced by deformation-modified precipitation of θ′-phase approximants in an Al–Cu alloy, Mater. Sci. Eng. A 676 (2016) 138–145, https://doi.org/10.1016/j.msea.2016.08.068.
[9] I.S. Zuiko, S. Mironov, R. Kaibyshev, Microstructural evolution and strengthening mechanisms operating during cryogenic rolling of solutionized Al–Cu–Mg alloy, Mater. Sci. Eng. A 745 (2019) 82–89, https://doi.org/10.1016/j.msea.2018.12.103.
[10] S. Lee, Z. Horita, S. Hirosawa, K. Matsuda, Age-hardening of an Al–Li–Cu–Mg alloy (2091) processed by high-pressure torsion, Mater. Sci. Eng. A 546 (2012) 82–89, https://doi.org/10.1016/j.msea.2012.03.029.
[11] Y. Tang, W. Goto, Sh Hirosawa, Z. Horita, S. Lee, K. Matsuda, D. Terada, Concurrent strengthening of ultrafine-grained age-hardenable Al–Mg alloy by means of high-pressure torsion and spinodal decomposition, Acta Mater. 131 (2017) 57–64, https://doi.org/10.1016/j.actamat.2017.04.002.
[12] M. Gazizov, R. Kaibyshev, Precipitation structure and strengthening mechanisms in an Al–Cu–Mg–Ag alloy, Mater. Sci. Eng. A 702 (2017) 29–40, https://doi.org/10.1016/j.msea.2017.06.110.
[13] K. Ma, H. Wen, T. Hu, T.D. Topping, D. Isheim, D.N. Seidman, E.J. Lavernia, J. M. Schoenung, Mechanical behavior and strengthening mechanisms in ultrafine grain precipitation-strengthened aluminum alloy, Acta Mater. 62 (2014) 141–155, https://doi.org/10.1016/j.actamat.2013.09.042.
[14] R.Z. Valiev, N.A. Enikeev, M.Y. Murashkin, V.U. Kazykhanov, X. Sauvage, On the origin of the extremely high strength of ultrafine-grained Al alloys produced by severe plastic deformation, Scripta Mater. 63 (2010) 949–952, https://doi.org/10.1016/j.scriptamat.2010.07.014.
[15] W. Chrominski, S. Wenner, C.D. Marioara, R. Holmestad, M. Lewandowska, Strengthening mechanisms in ultrafine grained Al–Mg–Si alloy processed by hydrostatic extrusion – influence of ageing temperature, Mater. Sci. Eng. A 669 (2016) 447–458, https://doi.org/10.1016/j.msea.2016.05.109.
[16] W. Chrominski, M. Lewandowska, Precipitation phenomena in ultrafine grained Al–Mg–Si alloy with heterogeneous microstructure, Acta Mater. 103 (2016) 547–557, https://doi.org/10.1016/j.actamat.2015.10.030.
[17] H. Jia, R. Bjørge, L. Cao, H. Song, K. Marthinsen, Y. Li, Quantifying the grain boundary segregation strengthening induced by post-ECAP aging in an Al–5Cu alloy, Acta Mater. 155 (2018) 199–213, https://doi.org/10.1016/j.actamat.2018.05.075.
[18] I. Zuiko, R. Kaibyshev, Effect of plastic deformation on the ageing behaviour of an Al–Cu–Mg alloy with a high Cu/Mg ratio, Mater. Sci. Eng. A 737 (2018) 401–412, https://doi.org/10.1016/j.msea.2018.09.017.
[19] K. Ma, T. Hu, H. Yang, T. Topping, A. Yousefiani, E.J. Lavernia, J.M. Schoenung, Coupling of dislocations and precipitates: impact on the mechanical behavior of ultrafine grained Al–Zn–Mg alloys, Acta Mater. 103 (2016) 153–164, https://doi.org/10.1016/j.actamat.2015.09.017.
[20] X. Sauvage, E.V. Bobruk, M.Yu Murashkin, Y. Nasedkina, N.A. Enikeev, R.Z. Valiev, Optimization of electrical conductivity and strength combination by structure design at the nanoscale in Al–Mg–Si alloys, Acta Mater. 98 (2015) 355–366, https://doi.org/10.1016/j.actamat.2015.07.039.
[21] P.N. Rao, Dh Singh, H.-G. Brokmeier, R. Jayaganthan, Effect of ageing on tensile behavior of ultrafine grained Al 6061 alloy, Mater. Sci. Eng. A 641 (2015) 391–401, https://doi.org/10.1016/j.msea.2015.06.036.
[22] D.A. Porter, K.E. Easterling, M. Sherif, Phase Transformations in Metals and Alloys, third ed., CRC Press, 2009.
[23] I. Zuiko, R. Kaibyshev, Aging behavior of an Al–Cu–Mg alloy, J. Alloys Compd. 759 (2018) 108–119, https://doi.org/10.1016/j.jallcom.2018.05.053.
[24] Y. Huang, J.D. Robson, P.B. Prangnell, The formation of nanograin structures and accelerated room-temperature theta precipitation in a severely deformed Al–4 wt. % Cu alloy, Acta Mater. 58 (2010) 1643–1657, https://doi.org/10.1016/j.actamat.2009.11.008.
[25] Y. Nasedkina, X. Sauvage, E.V. Bobruk, M.Yu Murashkin, R.Z. Valiev, N.A. Enikeev, Mechanisms of precipitation induced by large strains in the Al–Cu System, J. Alloys Compd. 710 (2017) 736–747, https://doi.org/10.1016/j.jallcom.2017.03.312.
[26] I. Zuiko, V. Kulitskii, R. Kaibyshev, Effect of pre-straining method on mechanical properties of thermo-mechanically processed Al–Cu–Mg alloy, Def. Diff. For. 385 (2018) 364–369. https://doi.org/10.4028/www.scientific.net/DDF.385.364.
[27] D. Tabor, The Hardness of Metals, Clarendon Press, Oxford, 1951.
[28] S.P. Ringer, B.T. Sofyan, K.S. Prasad, G.C. Quan, Precipitation reactions in Al–4.0Cu–0.3Mg (wt.%) alloy, Acta Mater. 56 (2008) 2147–2160, https://doi.org/10.1016/j.actamat.2007.12.046.
[29] P. Heugue, D. Larouche, F. Breton, R. Martinez, X.G. Chen, Evaluation of the growth kinetics of θ' and θ-Al_2Cu precipitates in a binary Al–3.5 Wt. Pct Cu alloy, Metall. Mater. Trans. A. 50 (2019) 3048–3060, https://doi.org/10.1007/s11661-019-05227-8.
[30] J. da Costa Teixeira, D.G. Cram, L. Bourgeois, T.J. Bastow, A.J. Hill, C. R. Hutchinson, On the strengthening response of aluminum alloys containing shear-resistant plate-shaped precipitates, Acta Mater. 56 (2008) 6109–6122, https://doi.org/10.1016/j.actamat.2008.08.023.
[31] D. Blavette, E. Cadel, A. Fraczkiewicz, A. Menand, Three-dimensional atomic-scale imaging of impurity segregation to line defects, Science 286 (1998) 2317–2319, https://doi.org/10.1126/science.286.5448.2317.
[32] C. Liua, Z. Ma, P. Ma, L. Zhan, M. Huang, Multiple precipitation reactions and formation of θ'-phase in a pre-deformed Al–Cu alloy, Mater. Sci. Eng. A 733 (2018) 28–38, https://doi.org/10.1016/j.msea.2018.07.039.
[33] Y. Zhang, S. Jin, P.W. Trimby, X. Liao, M.Y. Murashkin, R.Z. Valiev, J. Liu, J. M. Cairney, S.P. Ringer, G. Sha, Dynamic precipitation, segregation and strengthening of an Al–Zn–Mg–Cu alloy (AA7075) processed by high-pressure torsion, Acta Mater. 162 (2019) 19–32, https://doi.org/10.1016/j.actamat.2018.09.060.
[34] H. Jia, R. Bjørge, L. Cao, H. Song, K. Marthinsen, Yanjun Li, Quantifying the grain boundary segregation strengthening induced by post-ECAP aging in an Al–5Cu alloy, Acta Mater. 155 (2018) 199–213, https://doi.org/10.1016/j.actamat.2018.05.075.
[35] M. Mabuchi, K. Ameyama, H. Iwasaki, K. Higashi, Low temperature superplasticity of AZ91 magnesium alloy with non-equilibrium grain boundaries, Acta Mater. 47 (1999) 2047–2057, https://doi.org/10.1016/S1359-6454(99)00094-4.
[36] W. Xu, X.C. Liu, X.Y. Li, K. Lu, Deformation induced grain boundary segregation in nanolaminated Al–Cu alloy, Acta Mater. 182 (2020) 207–214, https://doi.org/10.1016/j.actamat.2019.10.036.
[37] Y. Amouya, S.V. Divinski, Y. Estrin, E. Rabkin, Short-circuit diffusion in an ultrafine-grained copper-zirconium alloy produced by equal channel angular pressing, Acta Mater. 55 (2007) 5968–5979, https://doi.org/10.1016/j.actamat.2007.07.026.
[38] M. Murayama, Z. Horita, K. Hono, Microstructure of two-phase Al–1.7 at% Cu alloy deformed by equal-channel angular pressing, Acta Mater. 49 (2001) 21–29, https://doi.org/10.1016/S1359-6454(00)00308-6.
[39] S.J. Kang, Y.-W. Kim, M. Kim, J.-M. Zuo, Determination of interfacial atomic structure, misfits and energetics of Ω phase in Al–Cu–Mg–Ag alloy, Acta Mater. 81 (2014) 501–511, https://doi.org/10.1016/j.actamat.2014.07.074.
[40] D. Shin, A. Shyam, S. Lee, Y. Yamamoto, J.A. Haynes, Solute segregation at the Al/θ′-Al_2Cu interface in Al–Cu alloys, Acta Mater. 141 (2017) 327–340, https://doi.org/10.1016/j.actamat.2017.09.020.
[41] H. Liu, I. Papadimitriou, F.X. Lin, J. LLorca, Precipitation during high temperature aging of Al–Cu alloys: a multiscale analysis based on first principles calculations, Acta Mater. 167 (2019) 121–135, https://doi.org/10.1016/j.actamat.2019.01.024.
[42] H. Liu, B. Bellón, J. LLorca, Multiscale modelling of the morphology and spatial distribution of θ′ precipitates in Al–Cu alloys, Acta Mater. 132 (2017) 611–626, https://doi.org/10.1016/j.actamat.2017.04.042.
[43] V.S. Krasnikov, A.E. Mayer, Dislocation dynamics in aluminum containing θ' phase: atomistic simulation and continuum modeling, Int. J. Plast. 119 (2019) 21–42, https://doi.org/10.1016/j.ijplas.2019.02.010.
[44] M.R. Ahmadi, E. Povoden-Karadeniz, L. Whitmore, M. Stockinger, A. Falahati, E. Kozeschnik, Precipitate strengthening of non-spherical precipitates extended in ⟨100⟩ or {100} direction in fcc crystals, Mater. Sci. Eng. A 590 (2014) 262–266, https://doi.org/10.1016/j.msea.2013.10.043.

[45] F.J. Nie, B.C. Muddle, Microstructural design of high strength aluminum alloys, J. Phase Equil. 19 (6) (1998) 543–551, https://doi.org/10.1361/105497198770341734.
[46] M. Gazizov, R. Kaibyshev, Precipitation structure and strengthening mechanisms in an Al–Cu–Mg–Ag alloy, Mater. Sci. Eng. A 702 (2017) 29–40, https://doi.org/10.1016/j.msea.2017.06.110.
[47] M. Gazizov, I. Zuiko, R. Kaibyshev, Effect of cold plastic deformation prior to ageing on creep resistance of an Al–Cu–Mg–Ag alloy, Mater. Sci. For. 794–796 (2014) 278–283. https://doi.org/10.4028/www.scientific.net/MSF.794-796.278.